ADVANCED MATERIALS

DOI: 10.1002/adma.200701336

Single Crystalline Boron Nanocones: Electric Transport and Field Emission Properties**

By *Xingjun Wang*, *Jifa Tian*, *Tianzhong Yang*, *Lihong Bao*, *Chao Hui*, *Fei Liu*, *Chengmin Shen*, *Changzhi Gu, Ningsheng Xu*, and *Hongjun Gao**

Since the discovery of carbon nanotubes by Iijima,[1] 1D nanomaterials have stimulated great interest because of their potential fundamental and practical applications in many areas such as material research, chemistry, physics and engineering, etc. Among the 1D nanomaterials, boron is specially attractive due to its special physical properties.[2,3] For example, boron is an electron-deficient nonmetallic element in the Periodic Table, and its bonding is a curious blend of types (unusual three-center sp^2 hybrid valence bond) found in metals and in nonmetals.[4] Moreover, boron is the third lightest solid element, but with a high melting point of 2300 °C, as well as a hardness close to diamond.[5,6] These unique features make boron and boron-related compounds attractive for various applications including high-temperature, lightweight coating, and high-temperature semiconductor electronic devices. Recently, some theoretical studies suggest the existence of layered, tubular, and fullerene-like boron solids, which possess many novel structural, electronic, and thermal properties.[7,8] For example, the proposed boron nanotubes possess a metallic-like density of states which could have a much better conductivity than carbon nanotubes and have potential applications in field emission and high-temperature electronic devices.[9] Despite the importance of boron nanotubes, there were little reports on the experimental synthesis of boron nanotubes, except a few reports on the synthesis of boron nanowires and nanobelts. Amorphous boron nanowires were first fabricated by chemical vapor transport method using boron, iodine, and silicon as precursor, and by radiofrequency magnetron sputtering of the target made of boron and boron oxide.[2,3,10] Li's group also grew amorphous boron nanowires using laser ablation of a boron target at high temperature of 1300 °C.[11] Crystalline boron nanowires were synthesized by chemical vapor deposition reaction of diborane (B_2H_6) in Ar gas on alumina substrates.[12] Zhang et al.[13,14] and Yun et al.[15,16] then prepared crystalline boron nanowires by laser ablation and thermal vapor transport processes, respectively. In recent years, crystalline boron nanobelts have been also synthesized by using laser ablation of high-purity boron pellets and by pyrolysis of B_2H_6 at low temperatures of 630–750 °C.[17,18] The electrical conductivity of the above 1D boron nanomaterials has been measured, and the results indicate that crystalline boron nanowires and nanobelts are semiconducting and exhibit electrical properties higher than those of elemental bulk boron.[19,20] However, as another important 1D boron nanomaterial, boron nanocones have not yet been reported although it is expected that 1D nanocones should have some better properties than nanowires and nanobelts.[21,22]

In this Communication we report the synthesis of boron nanocones using a simple chemical vapor deposition method of thermal evaporation of B/B_2O_3 powders precursors in an Ar/H_2 gas mixture at a reaction temperature of 1000–1200 °C. The field emission and electric transport properties of boron nanocones were measured to explore possible future applications in flat panel displays, semiconductor field emitters, and as nanoelectronics building blocks.

Figure 1a and b show scanning electron microscopy (SEM) images of boron nanocones grown on a Si(111) substrate at

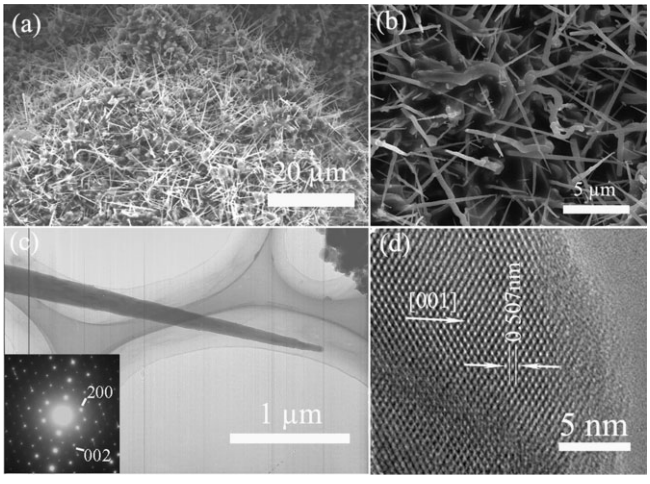

Figure 1. a,b) SEM images of boron nanocones, c) A typical TEM image of nanocone, the corresponding electron diffraction pattern (inset), d) HRTEM image of nanocone tip, showing crystalline structure and preferential growth along the [001] axis.

[*] Prof. H.-J. Gao, Dr. X. J. Wang, J. F. Tian, T. Z. Yang, L. H. Bao, C. Hui, C. M. Shen, Prof. C. Z. Gu
Beijing National Laboratory for Condensed Matter Physics
Institute of Physics, Chinese Academy of Sciences
Beijing 100080 (P.R. China)
E-mail: hjgao@aphy.iphy.ac.cn
Dr. F. Liu, Prof. N. S. Xu
State Key Laboratory of Optoelectronic Materials and Technologies
School of Physics and Engineering, Sun Yat-Sen University
Guangzhou 510275 (P.R. China)

[**] This work is supported in part by the National 863 (2007AA03Z305) and 973 (2007CB935503) projects, the National Science Foundation of China, and China Postdoctoral Science Foundation.

1100 °C for 2 h. The lengths of nanocones are several micrometers. The diameter of the nanocones reduces gradually from more than 300 nm at the root to a range of 50–100 nm at the tip. Similar products are also observed at reaction temperatures of 1000 and 1200 °C. Further sample characterization was carried out using transmission electron microscopy (TEM) and selected area electron diffraction (SAED). Figure 1c shows a low-magnification TEM image of a nanocone. Electron diffraction was done on different parts of the nanocone to determine its structure. The electron diffraction patterns at the different parts of the nanocone are the same, as shown in the inset of Figure 1c. It can be confirmed that the nanocone is single crystalline. The calculated lattice constants are a = 0.876 nm and c = 0.508 nm, which coincide closely with the values of α-tetragonal boron from the JCPDS database (73-0511).[23] Figure 1d shows a HRTEM image of nanocone tip. The boron nanocone tip is crystalline and covered by 1–2 nm thick amorphous layer. The preferential growth direction was determined to be the [001] direction. The outer amorphous layer is an oxide sheath, and formed when the crystalline boron nanocones were exposed in air. This is in agreement with previous results reported by other groups.[3,18]

Chemical compositions of the different parts of nanocone were analyzed by electron energy loss spectroscopy (EELS). Figure 2a depicts a typical EELS spectrum from the middle and root of the nanocone. The characteristic boron K-shell ionization edge was observed at about 188 eV. No oxygen, iron, or other impurities could be detected, as shown in the inset of Figure 2a. However, a very small amount of iron was detected by EELS from the front part of the nanocone (Fig. 2b). Considering the detection limitation of the EELS system, we can safely conclude that the oxygen content is below the detection limit of the EELS system. It is suggested that iron, as the catalyst, is located at the front part of the boron nanocone. Usually an iron cluster should be a dark spot in the HRTEM image. But no iron cluster was found in the HRTEM image of the nanocone tip (Fig. 1d). Iron should disperse uniformly in the tip of boron nanocone. The same sample was reanalyzed by EELS after exposing it in air for three months. Figure 2c is the EELS spectrum of the sample. A very weak oxygen peak at about 532 eV was detected, besides the characteristic boron peak at about 188 eV. Quantitative analysis showed that the amount of oxygen was about 6.0 at %. Xu et al.[18] reported 4.3 at % oxygen concentration in boron nanoribbons detected by EELS after exposing the samples in air for 64 days. The reason is that boron could be superficially oxidized in air at room temperature. Our result indicates that the oxidation starts from the surface of the boron nanocones. Figure 3 show the elemental mappings of boron, carbon, oxygen, iron, and silicon. It can be seen that only boron element was detected, indicating the formation of pure boron nanocones. Although the iron is found in the EELS spectrum at the nanocone tip, its absence in the mapping image suggests that the Fe nanoparticle size is too small to be resolved in the mappings.

The growth mechanism of amorphous and crystalline boron nanowires was postulated in previous work.[13,24] Approximate

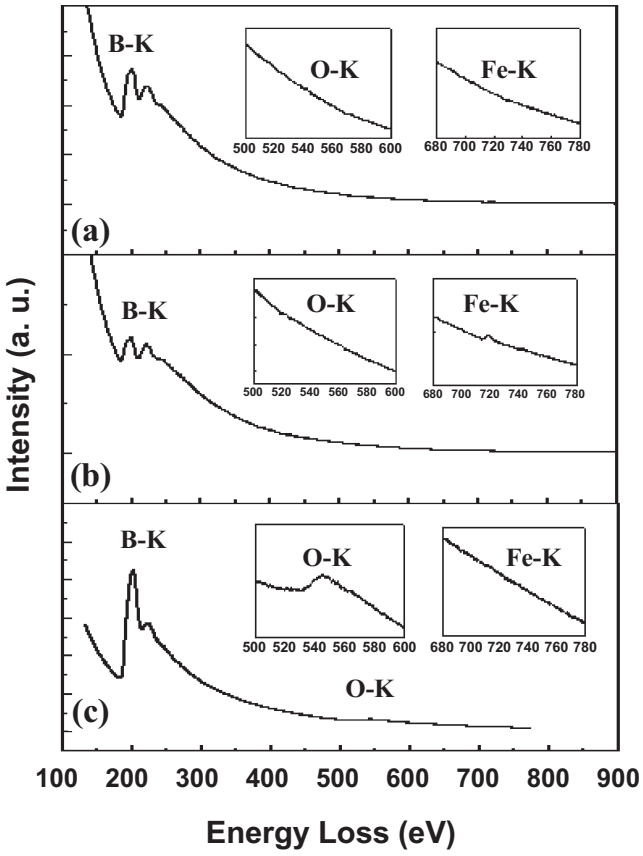

Figure 2. EELS spectra of the boron nanocones, a) A typical EELS spectrum from middle and root of nanocone. b) A typical EELS spectrum from the front part of nanocone. c) A typical EELS spectrum from middle and root of nanocone after exposing in air for three months.

oxide-assisted growth mechanism was used to interpret the growth of amorphous boron nanowires fabricated by magnetron sputtering of boron and B_2O_3 compound target.[24] The vapor-liquid-solid (VLS) mechanism was adopted to explain the growth of the crystalline boron nanowires, when Ni and Co nanoparticles served as the catalysts.[13] In our experiment, Fe_3O_4 nanoparticles were employed as the catalyst to fabricate the boron nanocones. We also attempted to synthesize boron nanocones without the Fe_3O_4 catalysts, but no 1D boron nanomaterials were found on the surface of Si(111) substrates. Moreover, the fact that iron was detected in the EELS spectrum only at the tips of the boron nanocones suggest that the Fe_3O_4 catalysts play a key role in the formation of boron nanocones and that a VLS mechanism is the most probable growth mechanism. Here, we give a description of the possible formation process of the boron nanocones. Firstly, B_2O_3 in the alumina boat transforms from solid to liquid as the temperature increases from 400 to 1100 °C. During the above process, B_2O_3 liquid reacts with solid boron in the alumina boat and forms dimeric boron monoxide (B_2O_2) vapor.[25] Meanwhile, iron and boron on the surface of Si(111) substrate serve as the energetically favored sites for the condensation and precipita-

ADVANCED MATERIALS

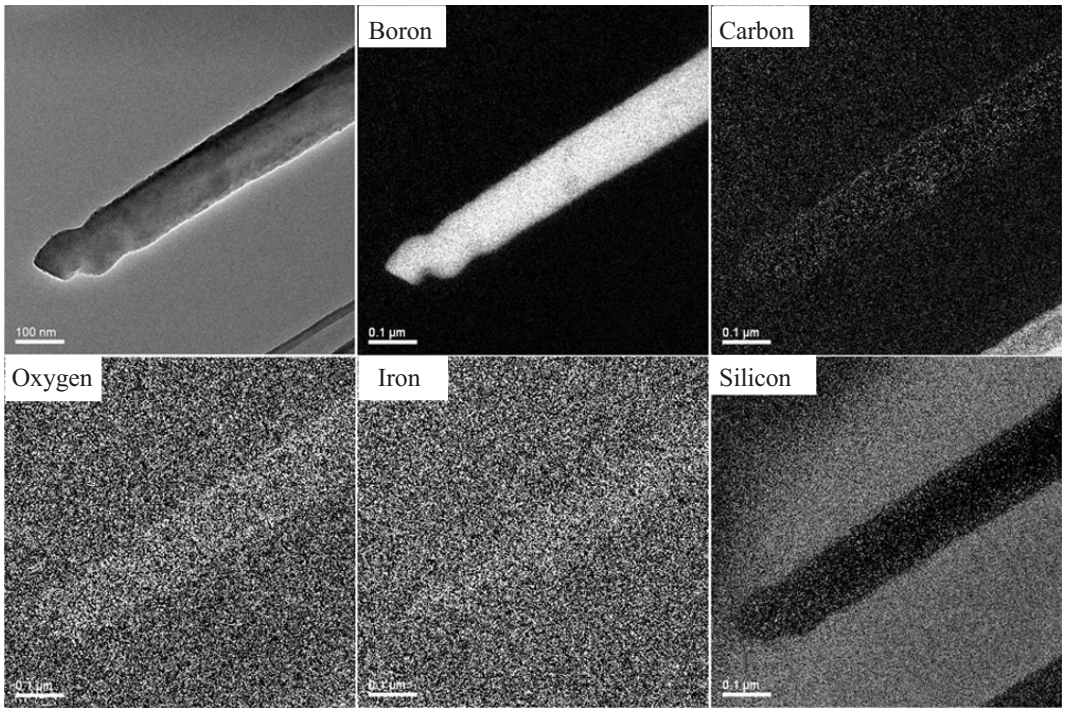

Figure 3. Elemental mappings of boron, carbon, oxygen, iron, and silicon.

tion of the reactant vapor. Iron and boron alloy nanoclusters are formed on the surface of Si(111) substrate. Then, the B_2O_2 vapor reacts with H_2 on the surface of the Si(111) substrate to form the boron. The condensation and precipitation of the boron species from the hot vapor takes place on these iron and boron alloy nanoclusters. 1D boron nanomaterials growth begins after boron species become supersaturated in the iron and boron alloy nanoclusters. At the initial stage, the abundant reactants provide sufficient boron vapor pressure to promote a rapid growth of the boron to form big nanodroplets in a short period of time. As the reaction goes on, pressure of the boron vapor is gradually reduced owing to the limited supply from the sources, leading to a transition from the nanodroplets into the nanocones.

Figure 4 shows SEM images of three boron nanocone devices with different diameters and lengths connected with Au electrodes. A typical boron nanocone device (Device 1) is illustrated in Figure 4a, the device length is about 3.1 μm, and the diameters of both ends of the device are about 110 and 190 nm, respectively. Figure 4b shows the second device (Device 2) with smaller diameter difference of both ends (length, 3.8 μm, diameters of the both ends, 240 and 280 nm). The third device (Device 3) has the approximately same diameter at both ends (length 2.5 μm, diameter 450 nm), as shown in Figure 4c.

Figure 5 illustrates room temperature current-voltage (*I–V*) curves of the above three devices in the voltage range of –20 V to 20 V. The inset represents *I–V* curves in the small voltage range of –1.0 V to 1.0 V. It can be seen that the *I–V* curve is symmetrical for Device 3. The current increases linearly from

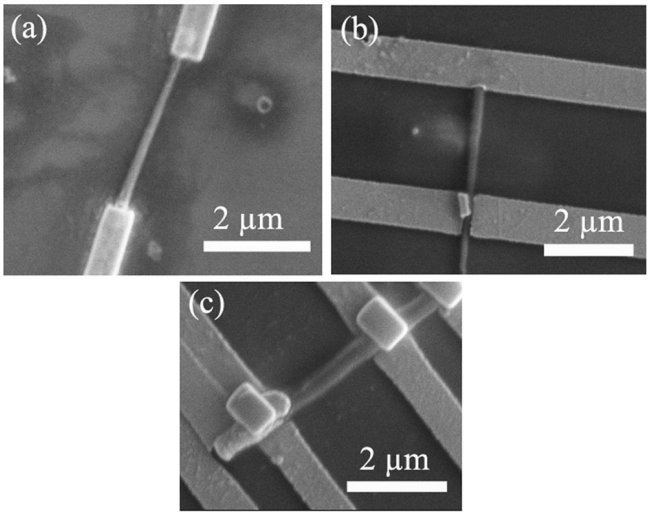

Figure 4. SEM images of three boron nanocone devices with different diameters and lengths connected with Au electrodes. a) Device 1 (length, 3.1 μm, the diameters of both ends, 110 nm and 190 nm). b) Device 2 (length, 3.8 μm, diameters of both ends, 240 nm and 280 nm). c) Device 3 (length, 2.5 μm, diameters of both ends, 450 nm).

–60 pA to 60 pA as voltage is raised from –1.0 V to 1.0 V, and the conductivity is calculated to be about 1.0×10^{-5} $\Omega^{-1}\cdot cm^{-1}$. The current saturates with further increasing the voltage above 1.0 V and decreasing the voltage below –1.0 V. Similar saturation tendencies are also found for Devices 1 and 2. However, the symmetrical curve shape is not observed for Devices 1 and 2. For Device 1, positive and negative satura-

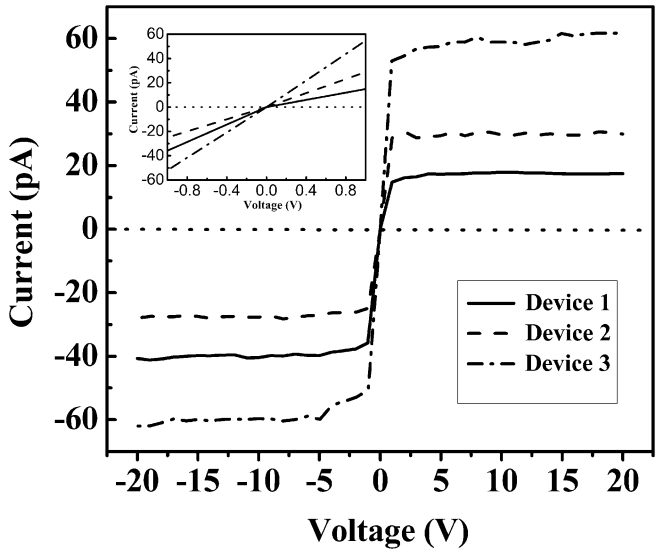

Figure 5. Room temperature current-voltage (*I–V*) curves of three devices at the voltage range of –20 V to 20 V, the inset is *I–V* curves at small voltage range of –1.0 V to 1.0 V.

tion currents are 20 pA and 40 pA, respectively. The conductivities are calculated to be 3.7×10^{-5} $\Omega^{-1}\cdot cm^{-1}$, and 7.3×10^{-5} $\Omega^{-1}\cdot cm^{-1}$ when the sectional area is approximately considered to be average value of the diameters of both ends of device. Positive and negative saturation currents are 32 pA and 27 pA for Device 2, and the conductivities are calculated to be 2.1×10^{-5} $\Omega^{-1}\cdot cm^{-1}$ and 1.8×10^{-5} $\Omega^{-1}\cdot cm^{-1}$, respectively. The conductivity values of $1.0–7.3 \times 10^{-5}$ $\Omega^{-1}\cdot cm^{-1}$ are ten times greater than that of pure bulk boron,[26] consistent with that of pure boron nanowires reported by Otten et al.,[12] and lower than that of Mg-doped boron nanobelts,[19] Ni diffused boron nanowires,[20] and C doped bulk boron.[26] It is suggested that the present boron nanocones are very pure, and the conductivity should be increased significantly when impurities such as Mg, V, and C, etc. are doped into boron nanocones. The asymmetric *I–V* curves for Devices 1 and 2 are attributed to the intrinsic character of boron nanocones. The boron nanowires and nanobelts with uniform size in whole length have the same carrier concentration and carrier mobility at the same positive and negative voltage, leading to the same export currents.[19,20] Device 3 with comparatively diameter size of both ends has the similar *I–V* curve shape with that of boron nanowires and nanobelts. However, the velocity excursion of carriers of boron nanocones for Devices 1 and 2 is different at the same positive and negative voltages due to the diameter size distinctness of both ends, resulting in the variety of carrier mobility, which leads to the different saturation currents. The saturation behaviors were also observed in other systems, such as carbon nanotube devices,[27,28] In_2O_3 nanowire transistors,[29,30] and Cd-doped ZnO nanowires varistors.[31] The saturation occurred at the positive voltage larger than 1.0 V and negative voltage smaller than –1.0 V for carbon nanotubes devices and Cd-doped ZnO nanowires varistors. The phonon scattering and density of states were used to explain this phenomenon.[27,31] Zhou et al.[29] reported that the saturation in In_2O_3 nanowires transistors was due to the local depletion of the electrons around the electrode at the positive voltage, leading to a saturation in the positive voltage region and an enhanced conductance in the negative voltage region. In contrast to the enhanced conduction, we observed saturation in the negative voltage, which is similar to that reported in carbon nanotubes devices and Cd-doped ZnO nanowires varistors. It is suggested that the saturation mechanism of boron nanocones is in analogous to that of the above two devices, and the current saturation of boron nanocones at the positive and negative voltages is due to phonon scattering and density of states of boron nanocones.

Figure 6 shows the *I–V* curves of Device 1 in the voltage range of 0 to 20 V at the different measurement temperatures from 5 K to 300 K. It can be seen that the line shape of all curves is similar with a saturation above ~1.0 V. The saturation current decreased with increasing temperature from 5 K to 300 K. It can be seen that the resistance increases with temperature for boron nanocones. Such positive temperature coefficient effect was first found in $BaTiO_3$ based ceramics by Heywang,[32] which was attributed to the change of potential barrier height at grain boundaries. Recently, a similar phenomenon was also observed in polycrystalline ZnO-based varistors[33] and Cd-doped ZnO nanowires varistors.[31] In addition, a model based on free carrier density approaching saturation, and electron mobility controlled by lattice scattering was developed to explain this effect.[33] At present, it is difficult for us to resolve clearly the mechanism of the positive temperature coefficient in the boron nanocones, and further studies are being carried out.

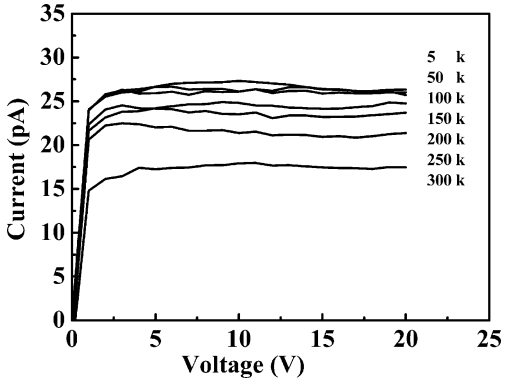

Figure 6. *I–V* curves of Device 1 in the voltage range of 0 V to 20 V at the different measurement temperature of 5 K to 300 K.

Figure 7 shows the current density versus the electric field *J–V* characteristics for the boron nanocones. Electric fields at the current densities of 10 μA cm^{-2} and 1 mA cm^{-2} are defined to be the turn-on and the threshold electric fields, respectively. For the boron nanocones, low turn-on and threshold electric fields of about 3.5 V μm^{-1} and 5.3 V μm^{-1} were

ADVANCED MATERIALS

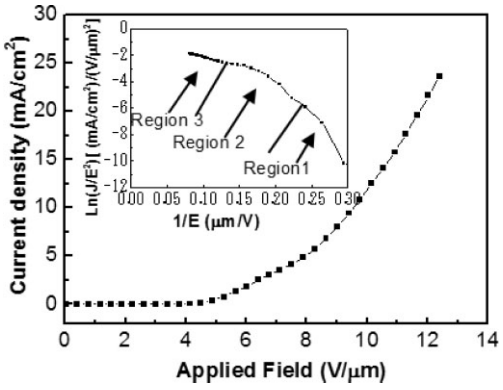

Figure 7. Field-emission *J–V* curve of boron nanocones, corresponding F–N plot, which is divided into three regions (inset).

observed. The emission current density was increased to 25 mA cm^{-2}, with no saturation tendency as the electric field was increased to 12 V μm^{-1}. The threshold field value is slightly higher than that reported for aligned carbon nantubes (1.6 V μm^{-1}),[34] close to that of tungsten oxide nanowires (6.2 V μm^{-1})[35] and ZnO nanopins (5.9 V μm^{-1}),[36] but lower than that of aligned ln_2O_3 nanowires (10.7 V μm^{-1}),[37] indicating that the prepared boron nanocones are indeed better field emitters.

The *J–V* relationship was analyzed by the Fowler–Nordheim (F–N) theory for semiconductors, which was described as Equation 1.[37,38]

$$J = A\left(\frac{\beta^2 E^2}{\phi}\right)\exp\left(-\frac{B\phi^{3/2}}{\beta E}\right)\exp\left(-\frac{\Delta W^s - \Delta W^p}{2kT}\right) \quad (1)$$

In the equation, J is the emission current intensity, E is the electric field, ϕ is the work function, A and B are constants, β is the so-called field enhancement factor, which reflects the ability of an emitter to enhance the local electric field at the tip as compared to the average macroscopic value, k is Boltzmann constant, T is the absolute temperature, ΔW^S is the increase of the surface potential barrier for semiconductor nanostructures due to surface states, and ΔW^P is the decrease of the surface potential barrier owing to field penetration. Figure 8 shows the diagram of energy bands near the surface of semiconductor nanostructures. E_c is the conduction band edge and E_F is Fermi level. The F–N plot is shown in the inset of Figure 4. It exhibits a nonlinear behavior in the measurement range of 0.07–0.30 μm V^{-1}. The $\ln(J/E^2)$ versus $1/E$ curve could be approximately divided into three regions for the field emission of boron nanocones. Region 1 corresponds to a low electric field (corresponding energy-band diagram shown in Fig. 8a), where field emission mainly depends on the surface states. With increasing the electric field, the surface potential barrier (ΔW^S–ΔW^P) decreases and the current increases rapidly. In Region 3 (corresponding energy-band diagram shown in Fig. 8b), the field penetration breaks down the surface potential barrier to dominant the field emission. Region 2 is a transition state between Regions 1 and 3, showing a competition between the surface states and the field penetration. Similar nonlinear characteristics of F–N plots were also found in In_2O_3 nanowires grown on InAs substrate.[37] In addition, high stability at a high emitting current was also exhibited by the present boron nanocones. An average emission current density of 25 mA cm^{-2} was set at a constant electric field of 12 V/μm and its fluctuations were recorded during 12 h. The fluctuation of the current density was less than ±3 %, and no obvious degradation was found during the period.

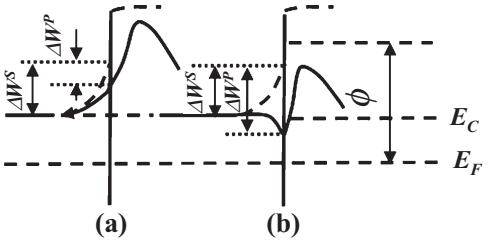

Figure 8. Diagram of the energy bands near the surface of semiconductor nanostructures, a) $\Delta W^S > \Delta W^P$, b) $\Delta W^S < \Delta W^P$.

In summary, large scale, high density single crystalline boron nanocones are fabricated by a simple chemical vapor deposition method. TEM and SAED show that the boron nanocone has the α-tetragonal boron structure with good crystallization. The VLS mechanism is the main formation mechanism of the boron nanocones. The result of field emission measurement shows a low turn-on and a threshold electric fields of about 3.5 V μm^{-1} and 5.3 V μm^{-1}. The electrical conductivity values of three boron nanocone devices are 1.0–7.3 × 10^{-5} $\Omega^{-1}.cm^{-1}$. The good electrical transport and field emission characteristics are attributed to the special properties of boron element. Boron nanocones with good electrical transport and field emission properties are promising candidates for application in flat panel displays and nanoelectronics building blocks.

Experimental

Preparation of Fe_3O_4 Nanoparticles: Fe_3O_4 nanoparticles with diameter less than 10 nm were synthesized by high temperature solution phase reaction of iron(III) acetylacetonate with 1,2-dodecandiol in the presence of oleic acid and oleylamine, which have been found in our previous publication [39].

Fabrication of Boron Nanocones: A horizontal tube furnace is used to synthesize one-dimensional boron nanomaterials in the experiments. Boron oxide (B_2O_3) powders (99.99 %) and boron powders (99.9 %) in a molar ratio of 1:5 were grounded together as precursors, which were charged into an alumina boat. The Fe_3O_4 liquid-drops were first spread over Si (111) wafer, a small amount of boron powders then were immerged into the Fe_3O_4 liquid-drops on Si (111) wafer. A mixture of boron and Fe_3O_4 nanoparticles coated Si (111) wafer was placed above the alumina boat as the substrate, which remained at out of reaction region before boron nanocones grew. The temperature, gas flow rate and evaporation rate of reaction region could be controlled. The boron nanocones grew by a two-step raising

temperature method. In the first procedure, when the temperature of reaction region reached 400 °C, the sample was transferred to reaction region rapidly and kept there for 30 min to eliminate the remained oleic acid and oleylamine. Then, the sample was returned to out of reaction region. A gas mixture of 95 % Ar and 5 % H_2 flow rate kept up 300 sccm through this procedure. In the second procedure, when the temperature of reaction region was increased to 1000–1200 °C, the sample was transferred to reaction region rapidly again. The growth of boron nanocones started. The reaction lasted for 1–4 hours in this procedure under a constant 50 sccm flow rate of 95 % Ar and 5 % H_2 gas mixture. During the above two processes, the gas pressure in tube was kept at atmospheric pressure. After the furnace was cooled to room temperature, dark brown or black products were found on the surface of Si(111) substrate.

Characterization of Boron Nanocones: Field-emission type scanning electron microscope (SEM) (XL-SFEG, FEI Corp.) was used for morphological observation of boron nanocones. Transmission electron microscopy (TEM) (Tecnai-20, PHILIPS Cop.) and high-resolution transmission electron microscopy (HRTEM) (Tecnai F20, FEI Corp.) with electron energy loss spectrometer (EELS) were employed to perform the microanalysis of boron nanocones. Electrical transport measurements were conducted using a home-built system with ≤ 1 pA noise under computer control. Firstly, boron nanocones were dispersed onto heavily doped thermally oxidized Si(111) wafer with an oxide layer (SiO_2) of 500 nm thickness. After drying the wafer and locating the boron nanocones position, about 100 nm Au electrodes were deposited at both ends of the boron nanocone by electron-beam lithography (EBL). The temperature dependence of the conductance was measured between 5 K and 300 K. Field emission experiments were carried out in a vacuum chamber with a base pressure of about 8×10^{-7} Pa at room temperature. The sample, as a cathode, was attracted to a stainless steel stand with conductive glue. A molybdenum probe of 1 mm^2 in tip area was adopted as an anode. The spacing of 200 μm between these two electrodes was controlled by a stepper. Emission current was measured by a picoammeter (Keithley 485). A ballast resistor of 10 MO was used to protect the apparatus against short-circuiting.

Received: June 3, 2007
Revised: August 6, 2007

[1] S. Iijima, *Nature* **1991**, *354*, 56.
[2] Y. Y. Wu, B. Messer, P. D. Yang, *Adv. Mater.* **2001**, *13*, 1487.
[3] L. M. Cao, Z. Zhang, L. L. Sun, M. He, Y. Q. Wang, Y. C. Li, X. Y. Zhang, G. Li, J. Zhang, W. K. Wang, *Adv. Mater.* **2001**, *13*, 1701.
[4] V. I. Matkovich, *Boron and Refractory Borides*, Springer, New York **1977**.
[5] D. Emin, *Phys. Today* **1987**, *4020*, 55.
[6] J. A. Kohn, *Boron Synthesis, Structure, and Properties*, Plenum, New York **1973**.
[7] I. Boustani, A. Quandt, *Europhys. Lett.* **1997**, *39*, 527.
[8] A. Gindulyte, W. N. Lipscomb, L. Massa, *Inorg. Chem.* **1998**, *37*, 6544.
[9] I. Boustani, A. Quandt, E. Hernandez, A. Rubio, *J. Chem. Phys.* **1999**, *110*, 3176.
[10] L. M. Cao, K. Hahn, Y. Q. Wang, C. Scheu, Z. Zhang, C. X. Gao, Y. C. Li, X. Y. Zhang, L. L. Sun, W. K. Wang, *Adv. Mater.* **2002**, *14*, 1294.
[11] X. M. Meng, J. Q. Hu, Y. Jiang, C. S. Lee, S. T. Lee, *Chem. Phys. Lett.* **2003**, *370*, 825.
[12] C. J. Otten, O R. Loune, M. F. Yu, J. M. Cowley, M. J. Dyer, R. S. Ruoff, W. E. Buhro, *J. Am. Chem. Soc.* **2002**, *124*, 4564.
[13] Y. J. Zhang, H. Ago, M. Yumura, T. Komatsu, S. Ohshima, K. Uchida, S. Iijima, *Chem. Commun.* **2002**, 2806.
[14] Y. J. Zhang, H. Ago, M. Yumura, S. Ohshima, K. Uchida, T. Komatsu, S. Iijima, *Chem. Phys. Lett.* **2004**, *385*, 177.
[15] S. H. Yun, A. Dibos, J. Z. Wu, D. K. Kim, *Appl. Phys. Lett.* **2004**, *84*, 2892.
[16] S. H. Yun, J. Z. Wu, A. Dias, X. Gao, U. O. Karlsson, *Appl. Phys. Lett.* **2005**, *87*, 113109.
[17] Z. K. Wang, Y. Shimizu, T. Sasaki, K. Kawaguchi, K. Kimura, N. Koshizaki, *Chem. Phys. Lett.* **2003**, *368*, 663.
[18] T. T. Xu, J. G. Zheng, N. Q. Wu, A. W. Nicholls, J. R. Roth, D. A. Dikin, R. S. Ruoff, *Nano Lett.* **2004**, *4*, 963.
[19] D. W. Wang, J. G. Lu, C. J. Otten, W. E. Buhro, *Appl. Phys. Lett.* **2003**, *83*, 5280.
[20] K. Kirihara, Z. Wang, K. Kawaguchi, Y. Shimizu, T. Sasaki, N. Koshizaki, K. Soga, K. Kimura, *Appl. Phys. Lett.* **2005**, *86*, 212101.
[21] C. X. Xu, X. W. Sun, *Appl. Phys. Lett.* **2003**, *83*, 3806.
[22] Z. X. Zhang, H. J. Yuan, J. J. Zhou, D. F. Liu, S. D. Luo, Y. Gao, J. X. Wang, S. S. Xie, *J. Phys. Chem. B* **2006**, *110*, 8566.
[23] JCPDS-International Centre for Diffraction Data, PCPDFWIN, v.2.4, **2003**.
[24] Y. Q. Wang, X. F. Duan, L. M. Cao, W. K. Wang, *Chem. Phys. Lett.* **2002**, *359*, 273.
[25] R. Z. Ma, Y. Bando, *Chem. Phys. Lett.* **2002**, *364*, 314.
[26] K. H. Hellwege, *Landolt-Bornstein Numerical Data and Functional Relationships in Science and Technology,* Springer, Berlin **1983**.
[27] Z. Yao, C. L. Kane, C. Dekker, *Phys. Rev. Lett.* **2000**, *84*, 29741.
[28] Y. X. Liang, Q. H. Li, T. H. Wang, *Appl. Phys. Lett.* **2004**, *84*, 3379.
[29] D. Zhang, C. Li, S. Han, X. Liu, T. Tang, W. Jin, C. Zhou, *Appl. Phys. Lett.* **2003**, *82*, 112.
[30] C. Li, D. Zhang, X. Liu, S. Han, T. Tang, J. Han, C. Zhou, *Appl. Phys. Lett.* **2003**, *82*, 1613.
[31] Q. H. Li, Q. Wan, Y. G. Wang, T. H. Wang, *Appl. Phys. Lett.* **2005**, *86*, 263101.
[32] W. Heywang, *Solid-State Electron.* **1961**, *3*, 51.
[33] D. Femandez-Hevia, J. de Frutos, A. C. Cabalero, J. F. Fernandez, *Appl. Phys. Lett.* **2003**, *82*, 212.
[34] M. Rao, D. Jacques, R. C. Haddon, W. Zhu, C. Bower, S. Jin, *Appl. Phys. Lett.* **2000**, *76*, 3813.
[35] Y. B. Li, Y. Bando, D. Golberg, *Adv. Mater.* **2003**, *15*, 1294.
[36] C. X. Xu, X. W. Sun, *Appl. Phys. Lett.* **2003**, *83*, 3806.
[37] S. Q. Li, Y. X. Liang, T. H. Wang, *Appl. Phys. Lett.* **2006**, *88*, 053107-1.
[38] R. Stratton, *Proc. Phys. Soc. B* **1955**, *68*, 746.
[39] T. Z. Yang, C. S. Shen, Z. A. Li, H. R. Zhang, C. W. Xiao, S. T. Chen, Z. C. Xu, D. X. Shi, J. Q. Li, H. J. Gao, *J. Phys. Chem. B* **2005**, *109*, 23233.